Yielding in colloidal gels: From local structure to mesoscale strand breakage and macroscopic failure

Himangsu Bhaumik [1], Tanniemola B. Liverpool [2], C. Patrick Royall [3,4,5] and Robert L. Jack [1,6]

[1] *Yusuf Hamied Department of Chemistry, University of Cambridge, Lensfield Road, Cambridge CB2 1EW, United Kingdom*

[2] *School of Mathematics, University of Bristol, Fry Building, Bristol BS8 1UG, United Kingdom*

[3] *HH Wills Physics Laboratory, Tyndall Avenue, Bristol BS8 1TL, United Kingdom*

[4] *School of Chemistry, University of Bristol, Cantock's Close, Bristol BS8 1TS, United Kingdom*

[5] *Gulliver UMR CNRS 7083, ESPCI Paris, Université PSL, 75005 Paris, France*

[6] *DAMTP, Centre for Mathematical Sciences, University of Cambridge, Wilberforce Road, Cambridge CB3 0WA, United Kingdom*

(Received 15 August 2024; revised 26 October 2024; accepted 28 April 2025; published 21 May 2025)

We report numerical simulations of creep flow and yielding of particulate depletion gels under constant shear stress, combining data on different length and time scales. We characterize the statistics of mesoscale strand-breaking events in the gel, which are distributed homogeneously in space, corresponding to macroscopically ductile flow. At the microscale, a spatiotemporal analysis of structural and mechanical metrics connects properties of strands before and after they fail, indicating that strand breakage is statistically predictable. Using results from different scales, we discuss the interplay between creeping and aging dynamics, and we demonstrate a viscosity bifurcation.

DOI: 10.1103/PhysRevE.111.055412

I. INTRODUCTION

Colloidal particles with attractive interactions can undergo gelation, forming kinetically arrested networks of strands [1–5]. These materials have widespread industrial applications, for example in food [6], paints [7], and biomedical engineering [8,9]. Gels are nonequilibrium systems whose properties depend strongly on their preparation and their history. Their rheology exhibits complex features typically seen in soft solids [10–13], and is also coupled to their characteristic coarsening and aging properties [14–17]. Such effects mean that the formulation of gel products is difficult to predict and control. For example, the delayed gravitational collapse of some gels poses important challenges for product shelf life [18–20].

From a theoretical and computational perspective, the prediction of gel properties is challenging because of a range of relevant length scales–macroscopic rheology and gel collapse depend on the (mesoscopic) gel strands, and these depend in turn on the individual particle interactions, which are the microscopic control parameters. An overarching theoretical challenge is to bridge scales from gels' microscopic structure to their rheology, presumably with mesoscale strands' behavior as an intermediate step. Important questions within this area include identification of relevant topological and mechanical features of the network of strands [15,21–26]; characterization of strand breakage [27–29] and its relation to macroscopic yielding [30–34]; understanding structural properties of strands and their dependence on microscopic particle interactions [5,35–38]; and connecting aging and sample history to its rheology [14,39–42].

In practice, colloidal gels span a range of interaction mechanisms, including highly directional "patchy" attractions [43], or very strong van der Waals interactions (e.g., in cement [44], which also features bond torsions due to particles' surface asperities). We focus here on depletion gels [4,5] where interactions are isotropic, with strengths comparable to the thermal energy k_BT, so that bond formation is reversible, and aging effects are significant [1,19]. These gels are formed by arrested spinodal decomposition, leading to strands of mesoscopic thickness, whose internal structure is similar to colloidal glasses. Their behavior is determined by a complex interplay between glassy phenomenology and phase separation, so that predicting gel properties from underlying particle interactions is extremely challenging [1,2,35,45]. Such materials are quite different from gels with van der Waals interactions, which form by (diffusion-limited) aggregation, leading to fractal structures whose strand thicknesses are only one or two particles [46,47], as also found in computational model gels with directional interactions [15,24,32].

The perspective of [30,31] is that yielding of gels takes place by stretching and breakage of strands. Individual breakage events have been simulated numerically [27–29], and observed in particle-resolved experiments [23]. Simulations of yielding in a model fractal gel [15] show similar events. In contrast to fractal gels that form by aggregation, depletion gels have weaker interactions, which are only a few times the thermal energy k_BT. Thermal fluctuations are strong enough for these bonds to break and reform during gelation, which leads to gel strands that are thicker than those formed by

aggregation. Bond breaking and formation continue after the gel has formed, allowing the system to evolve towards its equilibrium state (phase separation between particle-rich and particle-poor phases [4]). This leads to a significant time dependence in the gels' behavior, which is called physical aging. Yielding is also affected by particle motion within the strands [33], which depends in turn on their local structure and bonding. In particular, aging is related to a thickening of the gel strands [19,33,48,49], which can increase the yield stress [19].

In this work, we consider a quantitatively accurate simulation model of a depletion gel under applied shear stress [36,49,50]. We combine results on different length scales, to analyze yielding and failure. We characterize strand-breaking events using a statistical mechanical framework, based on extensive numerical data. We find distinctive structural signatures of strand breakage that manifest significantly before yielding, offering new possibilities for the prediction of gel behavior. Strand-breaking events are distributed homogeneously in space, indicating that the macroscopic yielding process has a ductile character, in contrast to the brittle behavior of fractal (irreversible) gels [32,34,51]. By considering the interplay of aging and macroscopic yielding, we also demonstrate a viscosity bifurcation in numerical simulations, complementing the experimental and theoretical perspectives of [14,39,40].

Together, these results–especially the systematic characterization of strand-breaking—represent an important step in bridging scales between microscopic local structure, mesoscopic strand-breaking events, and macroscopic rheology. We discuss how they pave the way for a unified theory of creeping and yielding in reversible gels, for example, via coarse-grained mesoscopic models.

The model is defined in Sec. II, with additional details in Appendix A. Our results are described in Sec. III with additional supporting material provided in various appendixes. Section IV summarizes the main conclusions, together with an outlook for future work.

II. MODEL

We simulate an established model of a size-polydisperse colloid-polymer mixture [33,35,36,41,49,50] that has been accurately mapped to the canonical two-component Asakura-Oosawa model [50,52]. We describe its main features, with full details in Appendix A. The depletion interaction between colloidal particles is modeled by a (truncated and shifted) nondimensionalized Morse potential

$$U_0(r) = \varepsilon_0[e^{-2\alpha_0(r-\ell_{ij})} - 2e^{-\alpha_0(r-\ell_{ij})} + c_{\rm sh}], \quad r \leqslant r_c, \quad (1)$$

where ℓ_{ij} is the average diameter of particles i and j; the well depth is ε_0 and the interaction range and cutoff parameters are $\alpha_0 = 33$ and $r_c = 1.4\ell_{ij}$. We take $U_0(r) = 0$ for $r > r_c$ and the shift $c_{\rm sh}$ is chosen such that $U_0(r_c) = 0$. We use nondimensionalized parameters throughout: the parameter ε_0 measures the interaction strength relative to $k_{\rm B}T$; the unit of time is $(m\bar{\ell}^2/k_{\rm B}T)^{1/2} = 1$ where $\bar{\ell}$ is the mean particle diameter, and the volume fraction is $\phi = \pi N\overline{\ell^3}/(6V)$ where N is the number of particles.

Colloid motion is overdamped within the solvent, which we simulate using Langevin dynamics with a large value of a (nondimensionalized) friction constant, $\lambda_0 = 10$. Previous work has shown that this simulation method is computationally efficient and accurate enough to capture the essential features of depletion gels [33,41], including quantitative comparisons with experiment [35,49]. However, we neglect hydrodynamic interactions, which do affect some aspects of gel structure [53,54].

Starting from a random configuration at $\phi = 0.2$, we prepare gels by simulating for a time $t_{\rm w}$, during which spinodal decomposition occurs. (We estimate the critical interaction strength for spinodal decomposition as $\varepsilon_0^* \approx 3.13$ [55]; we take $\varepsilon_0/\varepsilon_0^*$ in the range 1.5–7, always inside the spinodal.) Unless otherwise stated, results are shown for $t_{\rm w} = 3 \times 10^4$. After this waiting time, we use the method of [56,57] to impose a constant shear stress in the xy plane of nondimensionalized strength σ_0 (measured relative to $k_{\rm B}T/\bar{\ell}^3$), allowing flow along the x direction with Lees-Edwards boundary conditions. The interaction strength is $\varepsilon_{0,\rm prep}$ during the preparation and ε_0 during the shear. We mostly take $\varepsilon_{0,\rm prep} = \varepsilon_0$, which is the natural experimental condition (see, however, [58]). Unless otherwise stated we take $N = 10^4$; all results are averaged over many independent runs (typically 150), to enable statistically robust conclusions. The time t is measured from the start of shearing.

III. RESULTS

A. Flow, creep, and yielding

Figure 1 shows the behavior of gels under constant stress $\sigma_0 = 1$, for various interaction strengths ε_0 (with $\varepsilon_{0,\rm prep} = \varepsilon_0$). The average strain γ is plotted in Fig. 1(a) as a function of the time t since the start of shearing: for weak interactions, γ increases smoothly from zero, because the imposed stress is large enough to break the arms of the gel. For stronger interactions, there is an initial elastic deformation, followed by a plateau in γ, corresponding to a mechanically stable structure. At longer times, the gels creep, leaving the plateau with an upward slope. The oscillations at early times are due to the constant-stress simulation method, they do not affect the creep and yielding (see Appendix A; particularly, Fig. 11).

Figure 1(b) shows the average shear rate. For large ε_0, this decreases with time as the system enters the plateau, but the creeping motion means that it remains positive for all times. For intermediate ε_0, the rate initially decreases but later increases again, which corresponds to yielding of the gel, after some creep. The increasing $\dot{\gamma}$ in the flowing (post-yield) regime is a thixotropic response, which we attribute to disruption of the gel structure by the flow [10]. For small ε_0 there is no plateau in the stress and the shear rate is relatively large throughout. These dynamics are illustrated in Figs. 1(c)–1(e) for a weakly interacting gel that flows significantly in this time; Figs. 1(f)–1(h) show a strongly interacting gel undergoing creep, with very small structural changes. Note that weaker interactions allow spinodal decomposition to proceed more quickly, leading to thicker strands and larger pores at $t = 0$, which strongly influence the future evolution (see also Sec. III E, below).

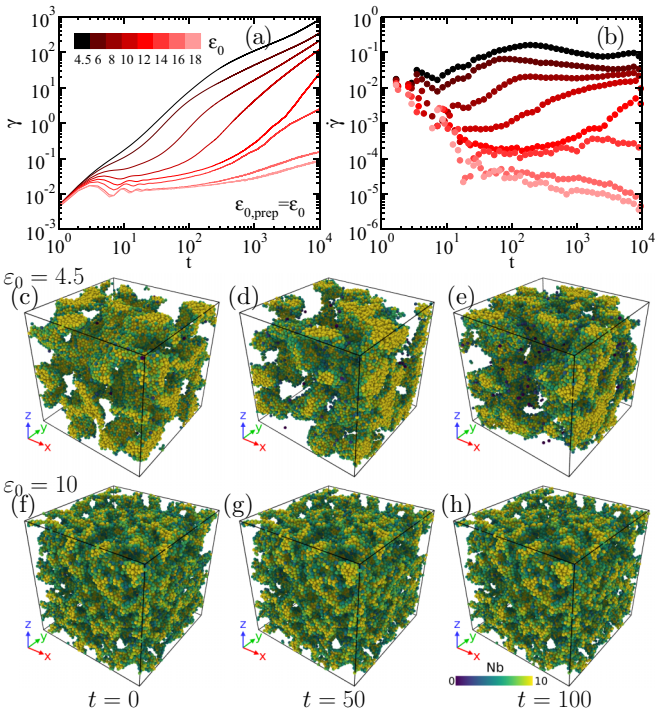

FIG. 1. (a) Strain γ as a function of time t, for gels with different interaction strengths ε_0, at fixed $\sigma_0 = 1$. (b) Corresponding strain rate, estimated from finite differences of the strain. (c)–(e) Snapshots for a gel with $\varepsilon_0 = 4.5$ at different times, as shown. Colors indicate the particle coordination N_b. (f)–(h) Similar snapshots for $\varepsilon_0 = 10$.

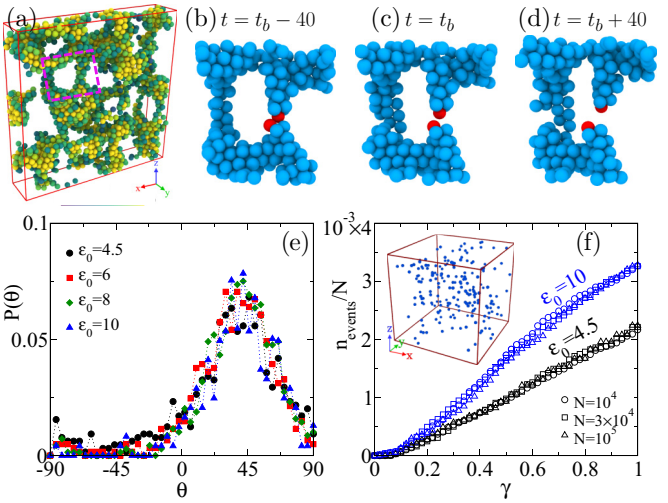

FIG. 2. (a) Rendering of a slice through a gel, to visualize the strands (coloring as in Fig. 1). (b)–(d) Expanded view of the boxed area highlighted in (a), showing a strand that breaks at time t_b. (e) Distribution of orientations of the breaking strands. (f) Number of strand-breaking events for two interaction strengths, varying the system size at fixed $\phi = 0.2$. Inset: locations in space of 300 representative events for a system with $N = 10^5$.

B. Statistical mechanics of strand-breaking events

Figures 1(c)–1(h) show that these gels are networks of strands, several particles thick. These are broken as the gel yields [30,31]. Breakage has been simulated for single strands [27–29]. This work analyzes it inside realistic gel networks, as illustrated in Figs. 2(a)–2(d), which focus on one strand, as it breaks. For a quantitative analysis, we introduce an algorithm that detects such events, based on network topology, inspired by Ref. [23]. We identify a breaking strand as a pair of particles [colored red in Figs. 2(b)–2(d)] for which the chemical distance (shortest bonded path) undergoes a sudden change. This approach distinguishes strand breakage from other processes where particles move apart; full details are given in Appendix B.

We analyze the statistics of thousands of such events, to understand yielding and flow. Figure 2(e) shows the distribution of strand orientations as they break: we project the interparticle vector in the xy plane, and define θ as the angle formed with the x axis. The distribution $P(\theta)$ is peaked around 45°, indicating that breaking strands are directed along the extensile direction of the shear flow.

Figure 2(f) plots the number of events as a function of strain, showing of order 10^{-3} events per particle per unit strain, independent of system size. This independence reflects that strand breakage is a localized event; it stands in contrast to sheared athermal solids where plastic events near yielding are size dependent [59]. We also find that weaker gels have fewer events: since their arms are thicker, a single event has more impact on the structure; the arms may also be more flexible, allowing more strain without breakage. The inset to Fig. 2(f) shows that strand-breaking events are distributed homogeneously in space, with no sign of shear banding or fracture [60]. Appendix C provides further data to support this homogeneity (see, in particular, Fig. 13). Consistent with the very weak finite-size effects, this indicates a macroscopically ductile response. Surprisingly, this differs from fractal (nonreversible) gels [32,34,51], whose behavior is more brittle.

C. Microscopic strand breaking

We characterize local structure in strand-breaking events that occur before macroscopic yielding ($\gamma < 1$ and $t < 400$). We characterize strands' local structure via their coordination numbers N_b, bond-orientational parameter q_2 [23], and the topological cluster classification (TCC) [61] from which we extract the number of tetrahedra (n_{tet}) and trigonal bipyramids (n_{tb}) in which particles participate. Full definitions of these structural measurements are given in Appendix D. The Supplemental Movie [62] illustrates structural evolution during creep.

Strand-breaking events are analyzed in Fig. 3, which plots averaged structural quantities as a function of time, measured relative to the strand-breaking events. That is, for each strand-breaking event, we compute the relevant structural quantities for the particles involved in the event. Denoting the time of the event by t_b, we average the results over all such events, as a function of $t - t_b$. These data are compared with the structural average over all particles. This reveals a consistent trend—strands that will break in the future already have nontypical structure for $t \approx t_b - 50$, characterized by fewer bonds (N_b), fewer locally favored structures ($n_{\mathrm{tet}}, n_{\mathrm{tb}}$), and increasingly elongated bond orientations (q_2). These preyielding effects are particularly pronounced for large ε_0, where the shear rates are also lowest. After the breaking event ($t > t_b$), these quantities

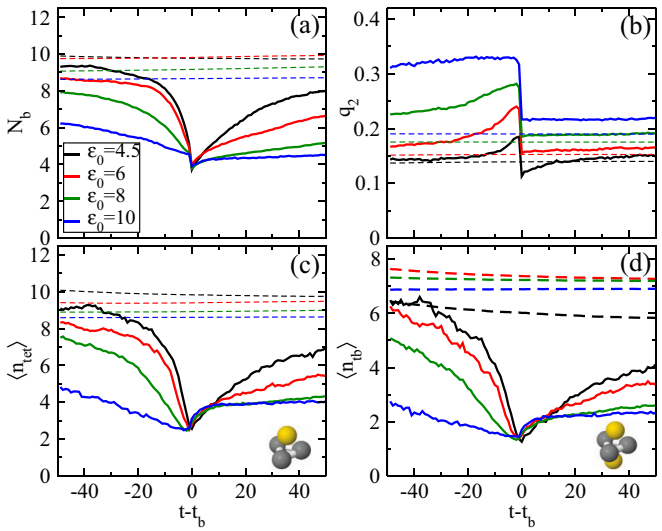

FIG. 3. (a) Averaged behavior of the coordination number N_b for particles involved in strand-breaking events, as a function of the time relative to the event. Dashed lines show the averaged behavior for all particles. Other panels show analogous results for (c) bond-order parameter q_2, (c),(d) numbers of tetrahedra and triangular bipyramids in which the particles participate.

tend back towards their bulk values, presumably because the stretched arm is no longer in tension and can relax locally. However, the local structures and N_b both remain nontypical, presumably because particles that were involved in strand breakage are likely to remain near the surface of gel strands.

These results rely on our algorithm for reliable identification of strand-breaking events, and on the ensuing statistical analysis. Together, these methods show that mesoscopic dynamics is *statistically predictable* based on microscopic structural measurements, which already differ from their typical values before breakage occurs. This offers a potential route towards material design and control of yielding.

Figure 4 shows a similar analysis for quantities associated with the plasticity and mechanical properties of the system. To this end, we consider nonaffine displacement per particle D^2_{min} and the stress anisotropy J_2 as defined in Appendix D. Figure. 4(a) shows the nonaffine displacement D^2_{min} [63] over a short time period $\Delta t = 1$, for particles involved in strand

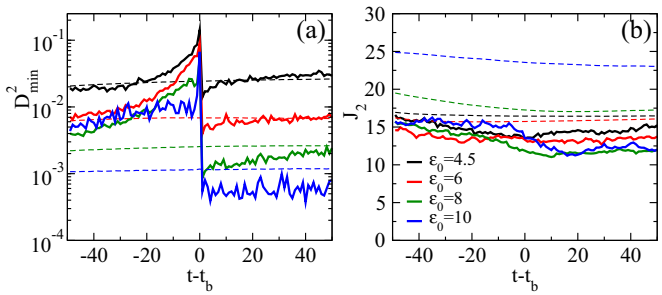

FIG. 4. Averaged behavior of (a) nonaffine displacement D^2_{min} and (b) stress anisotropy J_2, for particles involved in strand-breaking events, as a function of the time relative to the event. Dashed lines show the averaged behavior for all particles.

breaking. As expected, D^2_{min} shows a peak when strands break. Note that D^2_{min} starts to increase significantly before the breakage event, especially for weaker interactions. We attribute this to a thinning and partial fluidization of the arm before failure, as observed for isolated single strands [29]. Figure 4(b) shows the local Irving-Kirkwood [64] stress anisotropy J_2 [29]: this does not change rapidly at the breaking time but for larger ε_0 one sees that particles have lower J_2 during strand breakage (solid lines), compared with the average (dashed). This is again consistent with partial fluidization relaxing the residual stresses in the arms, before breakage [29].

As an additional illustration of strand breaking, Fig. 5 shows the variation of different quantities during a representative event. The strand is initially very thick ($t = t_b - 40$, before breaking). As time elapses the quantities change: the strand becomes thinner (smaller N_b) in the vicinity of the point where it is going to break; it also becomes more stretched (larger q_2), and its behavior is more liquidlike (smaller stress anisotropy J_2). A larger D^2_{min} value around the location indicates the region undergoes more plastic displacement while it breaks. (See also the Supplemental Movie [62].)

D. Viscosity bifurcation

Having analyzed the microscopic structure and mesoscopic strands, we now turn to macroscopic rheology. Recall that depletion gels are far-from-equilibrium states so their structure tends to descend slowly in the energy landscape. For gels and indeed colloidal glasses under shear, this can lead to a bifurcation similar to those found in [10,14,30,31,39,40]: aging strengthens the gel, which suppresses strand breaking and allows further aging; on the other hand, if too many strands are broken, then aging is interrupted and the gel weakens, promoting further breakage and yielding.

To see this effect, we fix the interaction strength and perform additional simulations in which we vary the imposed stress σ_0. Figures 6(a) and 6(b) show the average strain and compliance [$J = \gamma/\sigma_0$] as a function of time, for $\varepsilon_0 = 10$. We observe a data collapse for small σ_0 in Fig. 6(b), showing that a linear-response regime exists for the solidlike response to shear.

Using finite differences to estimate the strain rate from the data of Fig. 6, we show in Fig. 7(a) the effective viscosity $\eta = \sigma_0/\dot{\gamma}$ (this is the ratio of applied stress to measured shear rate). For small stress, the viscosity increases smoothly due to aging. For larger stress, the viscosity initially increases, but strand-breaking events become important at later times, and it reduces. This is the viscosity bifurcation [14,39,40]. (These results have similarities to [33], particularly the "older" gels discussed in that work.)

For the time $t = 10^4$ considered in Fig. 7(a), we identify a (weakly time-dependent) yield stress $\sigma_{y,t} = 0.7$: an arrow separates samples above and below this value. For longer times, systems in the arrested state may eventually yield, so $\sigma_{y,t}$ tends to decrease with time. This situation is generically expected in systems where thermal fluctuations are significant, since all stressed states are inherently metastable [65]. The signature of the viscosity bifurcation in such cases is that the yield process is significantly delayed, because the gel is strengthened during aging.

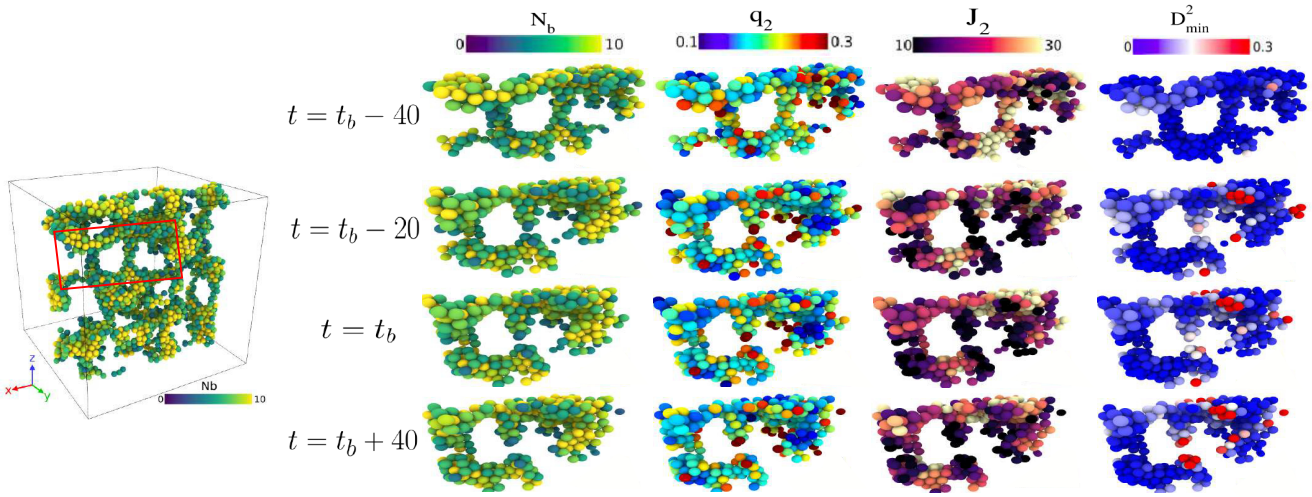

FIG. 5. Left: Rendering of a slice through a gel, to visualize the strands for $\varepsilon_0 = 10$. The highlighted boxed area denotes the particular strand whose evolution we will monitor around the breaking time t_b. Particles are colored according to the value of different metrics, as indicated. See also the Supplemental Movie [62].

Following [57], we also consider the sample-to-sample fluctuations of the strain as a function of γ: its (time-dependent) variance is

$$(\Delta\gamma)^2 = \frac{\langle\gamma^2(t)\rangle - \langle\gamma(t)\rangle^2}{\langle\gamma(t)\rangle^2}. \tag{2}$$

Figure 7(b) plots this variance parametrically as a function of $\gamma = \langle\gamma(t)\rangle$. The variance shows a maximum at the yielding point of the gel, and the strain at this point is always $\gamma_c \approx 0.4$. For each numerical simulation, we extract the time taken to reach this critical strain: the failure time t_f is the average of these random times (the full distribution of times is discussed below). On computing this time as a function of both σ_0 and ε_0, Fig. 7(c) shows (as expected) that the failure time increases as stress is reduced. In addition, this effect is mostly determined by the ratio σ_0/ε_0 of shear stress to bond strength. It can be fitted as $t_f \sim (\sigma_0 - \sigma_\infty)^{-\alpha}$ where $\alpha \approx 2.4 \pm 0.1$ for all ε_0. (We fit using α independent of ϵ_0 for convenience: other choices would be possible but our results are not sufficient to determine the dependence of α on model parameters; see also [66].)

We also observe that $\sigma_\infty/\varepsilon_0$ increases weakly with ε_0. This dependence must be due to thermal fluctuations since for an athermal system, dimensional analysis shows that σ_∞ must be proportional to ε_0. (The only stress scale in that case would be the bond strength ε_0 divided by the particle volume.) This means that the results for t_f in Fig. 7(c) would collapse onto a single curve in an athermal system. For the larger values of ε_0 the data do almost collapse, indicating that these systems are close to the athermal regime. However, thermal effects are clearly significant for the smaller bond strengths. Comparing with [30], we do not find evidence for a two-step breaking process. we attribute this to the weaker bonds in our depletion gels so that thermal fluctuations are essential, and particles may also rearrange within strands as the system is strained.

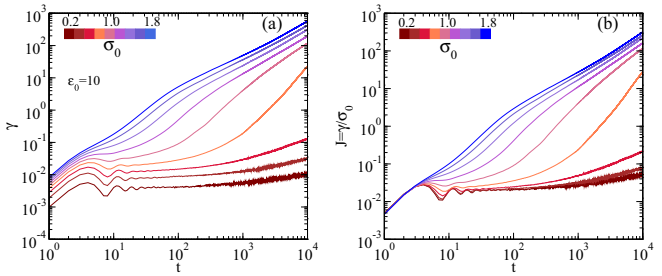

FIG. 6. (a) Strain vs time and (b) compliance $J = \gamma/\sigma_0$ vs time, for various imposed stresses σ_0, at $\varepsilon_0 = 10$.

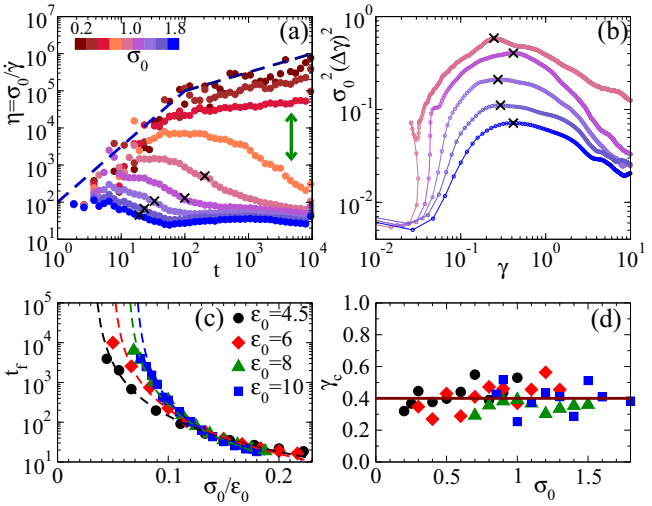

FIG. 7. (a) Effective viscosity $\eta = \sigma_0/\dot{\gamma}$ against time, varying the imposed stress σ_0 at fixed $\varepsilon_0 = 10$. Dashed lines indicate $\eta \sim t$ and $\eta \sim t^{0.5}$ for short and long times, respectively. The green arrow indicates the bifurcation at $\sigma_0 \approx 0.7$. (b) Normalized strain fluctuations plotted against the average strain γ for different σ_0 [color code shared with (a)]. Black stars indicate the maxima, which are interpreted as critical strains γ_c [these points are also indicated in (a)]. (c) Failure time t_f against imposed stress, with power-law fits shown as dashed lines. (d) Critical strains for all σ_0, ε_0 have $\gamma_c \approx 0.4$ [coloring shared with (c)].

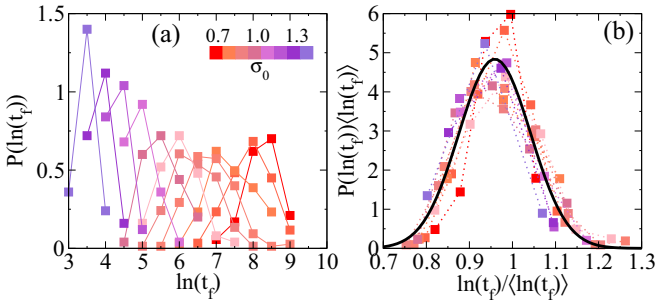

FIG. 8. Failure times for $\epsilon_0 = 10$. (a) Distribution of failure time obtained from different samples, as a function of σ_0. (b) Scaled distribution showing data collapse. The solid line is a Gaussian fit.

the strands can then break via a necking instability [29], which is distinct from the scenario of [30].

Figure 7(d) shows that γ_c depends weakly on ε_0, as already noted above. For each sample k, we can also define the individual failure time as $t_f^{(k)}$, the time at which $\gamma = \gamma_c$. Averaging over samples gives the average failure time t_f discussed above. In Fig. 8 we show the distributions of these times. As expected, the peak of the distributions decreases with increasing σ_0 while keeping their Gaussian form. While rescaled with their mean, we find a nice collapse of data as shown in Fig. 6(b). A similar scaling form has also been observed for the creeping of amorphous solid under tensile force [67] (see also [30]).

E. Effects of gel preparation

The properties of these gels depend on the protocol used to prepare them. To explore this, we performed additional simulations where we varied the waiting time t_w before the shear stress is applied, as well as $\varepsilon_{0,\text{prep}}$ (interaction strength during the waiting time), while keeping fixed the interaction strength ε_0 during the shear.

These different protocols lead to different gel structures. To characterize this, we measured distributions of strand diameters and pore sizes, following [68]. These results are obtained at $t = 0$, before any shear stress is applied (see Appendix E for further details of the numerical method). Figures 9(a)–9(d) show that larger t_w and smaller $\varepsilon_{0,\text{prep}}$ result in thicker strands and larger pores inside the gel. The increasing length scales as a function of t_w are consistent with the expected coarsening of the gel structure during the preparation time. At fixed t_w, increasing $\varepsilon_{0,\text{prep}}$ tends to reduce the pore diameter and strand thickness; this is expected because strong interparticle attractions hinder particle motion, which requires thermal activation.

We also measure the number of neighbors per particle, and the total energy for a gel prepared with different $\varepsilon_{0,\text{prep}}$. As shown in Figs. 9(e) and 9(f), their variation with t_w again reveals the annealing behavior, with a more stable structure as t_w increases.

On subjecting these gels to constant stress, the number of strand-breaking events is shown in Fig. 9(g), plotted parametrically against the strain. Gels with larger t_w experience fewer strand-breaking events than those with smaller t_w [this is expected by analogy with Fig. 2(f) in that gels with thicker strands feature fewer events]. Additional results for the creeping behavior of these samples are given in Appendix E; in particular, Fig. 14.

The key results from this analysis are summarized in Fig. 10, which shows results for the strain, and for the failure

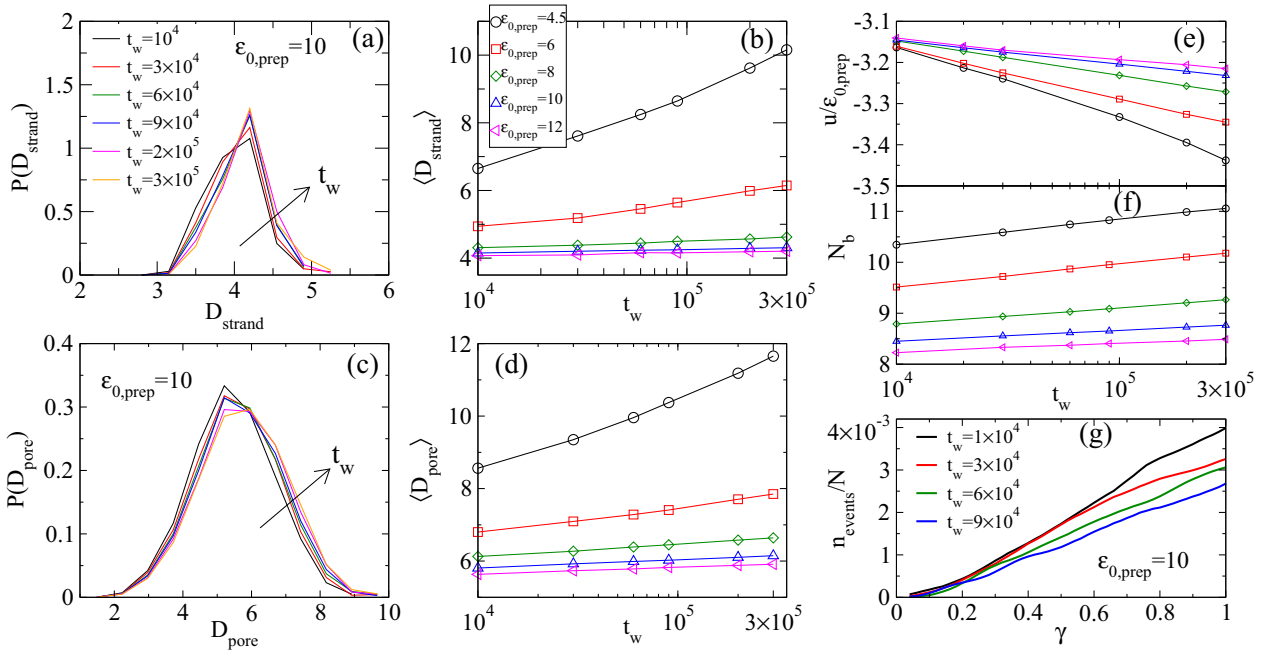

FIG. 9. Effect of t_w: Distribution of (a) strand thickness and (c) pore size for a gel with $\varepsilon_{0,\text{prep}} = 10$ for different waiting time t_w. (b) Average strand thickness and (d) average pore diameter as a function of t_w for different $\varepsilon_{0,\text{prep}}$. (e) Total energy per particle and (f) the average number of neighbors as a function of t_w for different $\varepsilon_{0,\text{prep}}$. (g) Number of breaking events as a function of accumulated strain for different t_w for a gel with $\varepsilon_{0,\text{prep}} = \varepsilon_0 = 10$. [(a) shares color coding with (c); also (b),(d), (e), and (f) share the same color code.]

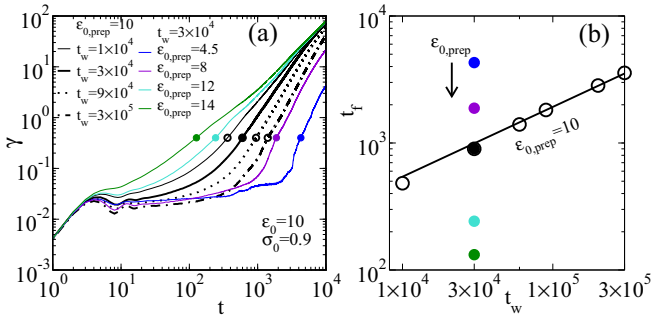

FIG. 10. (a) Strain against time for gels prepared with different t_w (all with $\varepsilon_{0,\mathrm{prep}} = 10$) and for different $\varepsilon_{0,\mathrm{prep}}$ (all with $t_w = 3 \times 10^4$). Dots mark times t_f at which $\gamma = 0.4$. (b) Failure times t_f increase with t_w and decrease with $\varepsilon_{0,\mathrm{prep}}$. The straight line indicates $t_f \sim t_w^{1/2}$. [Color coding for $\varepsilon_{0,\mathrm{prep}}$ is shared with (a).]

time t_f, extracted by the same method used in Fig. 7. This failure time increases significantly with t_{prep}, which reflects the fact that coarsening occurred during preparation. (Coarsening leads to thicker arms, and shifts the competition between aging and strandbreaking.) Overall, coarsening during preparation tends to suppress the stress-induced yielding, and shifts the viscosity bifurcation to larger stress. This reveals a connection between a coarser mesoscopic gel structure and a more robust macroscopic material. The data fits well to $t_f \sim t_w^{1/2}$, which differs from the (so-called) universal scaling $t_f \sim t_w$, found experimentally in fractal gels [46], providing further evidence that these depletion gels behave differently.

IV. CONCLUSION

We have analyzed creeping and yielding in a model depletion gel, including behavior on different length and time scales. The yielding process relies on the breakage of mesoscale strands (Fig. 2): we showed how individual breaking events can be identified, and that they are distributed homogeneously in space. At the microscopic scale we characterized the local structure of breaking strands (Figs. 3–5), including a predictive relationship between this structure and the breaking events. At the macroscale, the homogeneous distribution of breakage events corresponds to a ductile response.

These connections between scales rely on the relatively thick strands in these weak (depletion) gels, in contrast to fractal gels formed by aggregation, where the strands are much thinner [32,46]. Despite recent advances towards generic theories of gels [24,25], our results reveal a more nuanced picture, in which different types of particulate gel behave differently. A more detailed comparison between simulations of weak and fractal gels would be valuable, to disentangle model-specific and universal features.

Our results also offer several opportunities for future progress. By uncovering relationships between strand-breaking events and microscopic structure, we offer a route towards the "bottom-up" design of particulate gels, through their microscopic interactions. It would also be interesting to relate strands' behavior near the viscosity bifurcation to the theoretical models that describe these phenomena at macroscopic scale [40,69]. Based on of Fig. 2, one may also propose an elastoplastic model [70] to capture the interdependence of different strand breakage events, whose microscopic properties would be encapsulated by model parameters. Finally, the dependence of failure time t_f on $\varepsilon_{0,\mathrm{prep}}$ and t_w offers interesting opportunities for control of gel properties via their preparation conditions, including nontrivial protocols involving time-dependent interactions [58,71], and combining measurements with feedback protocols [72,73].

ACKNOWLEDGMENTS

We thank Suzanne Fielding, Malcolm Faers, Kris Thijssen, Abraham Mauleon-Amieva, and Rui Cheng for helpful discussions. This work was supported by the EPSRC through Grants No. EP/T031247/1 (H.B. and R.L.J.) and No. EP/T031077/1 (C.P.R. and T.B.L.). C.P.R. is also grateful to the Agence National de Recherche of France for support via the grant DiViNew.

APPENDIX A: DETAILS OF SIMULATION METHODS

This Appendix provides additional details of our simulation methodology.

1. Equations of motion

We simulate N particles with mass m and velocities $\boldsymbol{v}_i$, evolving with Langevin dynamics in a cubic simulation box of volume L^3, with periodic boundaries. We consider a Morse potential $U(r)$ that mimics the short-ranged depletion interaction. Hence, the position $\boldsymbol{r}_i$ of particle i obeys $d\boldsymbol{r}_i/dt = \boldsymbol{v}_i$, and

$$m\frac{d\boldsymbol{v}_i}{dt} = -\nabla_i V - \lambda\left(\boldsymbol{v}_i - \boldsymbol{u}_i^{\mathrm{aff}}\right) + \sqrt{2\lambda k_{\mathrm{B}}T}\,\boldsymbol{\xi}_i, \qquad \text{(A1)}$$

where $V = \sum_{1\leqslant i<j\leqslant N} U(|\boldsymbol{r}_i - \boldsymbol{r}_j|)$ is the total potential energy, λ is the friction constant, $\boldsymbol{u}_i^{\mathrm{aff}}$ is the local velocity of the (implicit) solvent, and $\boldsymbol{\xi}$ is a standard Gaussian white noise. (In the absence of shear flow $\boldsymbol{u}_i^{\mathrm{aff}} = 0$, the sheared case is discussed below.) The velocity damping time is $\tau_d = m/\lambda$.

We nondimensionalize the system using the mean particle diameter $\bar{\ell}$ and the natural time scale $\tau = (m\bar{\ell}^2/k_{\mathrm{B}}T)^{1/2}$, and taking $k_{\mathrm{B}}T$ as the energy scale. Then the nondimensionalized Morse potential is $U_0 = U/(k_{\mathrm{B}}T)$ as defined in the main text. note that α_0 is the corresponding nondimensionalized range parameter. The nondimensionalized friction is $\lambda_0 = \lambda\tau/m$; we take $\lambda_0 = 10$ to mimic overdamped dynamics. The integration time step is $\Delta t = 0.001\tau$. To avoid crystallization we consider a size polydisperse system. We have taken seven types of particles with diameters equally spaced between $0.88\bar{\ell}$ and $1.12\bar{\ell}$, with relative concentrations

$$[0.0062, 0.0606, 0.2417, 0.3829, 0.2417, 0.0606, 0.0062]$$

to mimic a Gaussian distribution of diameters. For colloidal motion, a natural time scale is the Brownian time $\tau_B = \bar{\ell}^2\lambda/(24k_{\mathrm{B}}T)$, which is the typical time for an overdamped free particle to diffuse its radius. For the parameters chosen here, $\tau_B = 0.417\tau$. All simulations are performed in LAMMPS [74].

As described in the main text, gels are prepared by simulation from a random initial condition at volume fraction ϕ

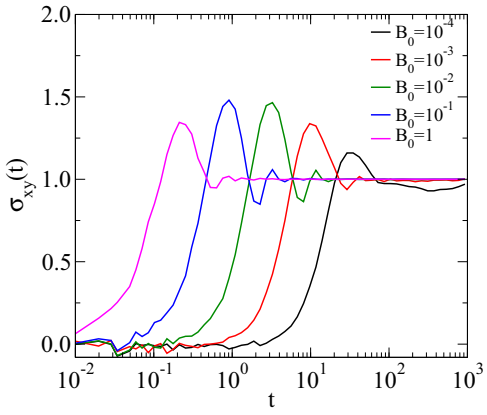

FIG. 11. Virial stress (xy component) as a function of time for different damping parameter B_0 while a gel ($\varepsilon_{0,\mathrm{prep}} = \varepsilon_0 = 10$) is subjected to the constant stress shear protocol with $\sigma_0 = 1$. For small B_0, the system takes a long time to relax to the desired stress σ_0.

for a time t_w, in the absence of shear. After this preparation, we apply a constant shear stress σ in the xy plane as in [56,57], with flow along the x direction. The corresponding nondimensionalized stress is $\sigma_0 = \sigma\bar{\ell}^3/(k_\mathrm{B}T)$. This is maintained through a feedback control scheme that is implemented [56,57] as

$$\partial_t\dot{\gamma} = B[\sigma_0 - \sigma_{xy}(t)], \tag{A2}$$

where $\dot{\gamma}$ is the shear rate and σ_{xy} is the observed (nondimensional) shear stress (measured from the virial) and B is the damping parameter determining how quickly internal stress relaxes to imposed value. We implement the shear with Lees-Edwards boundary conditions and the solvent velocity $\boldsymbol{u}_i^{\mathrm{aff}}$ points in the x direction, with magnitude $y_i\dot{\gamma}$, where y_i denotes the y component of $\boldsymbol{r}_i$. The dimensionless parameter $B_0 = B\tau^2$ determines how fast the shear rate responds to changes in stress. As discussed in [56,57], this should be fast enough that the stress remains constant on the slow time scales associated with creeping and yielding. We take $B_0 = 0.01$, which is large enough for our purposes, because the creeping flow is slow. Figure 11 shows the stress evolution starting from a quiescent state, showing that σ_{xy} converges to σ_0 on a time of order 1. (Increasing B makes the convergence faster, as expected.) The overshoot in σ_{xy} is due to the second-order dynamics [Eq. (A2)]. this effect also appears in the short-time oscillations of γ in Fig. 1(a).

Overall, the system evolves by integrating the equations of motion (A1) and (A2) simultaneously to calculate the particle velocities and the strain rate, with the strain imposed via the Lees-Edwards boundary conditions.

2. Dimensionless parameters and comparison with experiments

We briefly summarize the dimensionless parameters that determine the system behavior. The interaction potential has strength ε_0 and range α_0. The colloidal volume fraction is $\phi = \pi N\bar{\ell}^3/(6V)$. The preparation of the colloidal gel involves a (dimensionless) time t_w during which the network of strands forms. The applied shear stress is σ_0 and the parameter B_0 determines the rate of relaxation of the observed stress to its target value σ_0.

We fix $\alpha_0 = 33$, $\phi_0 = 0.2$, comparable with experimental gels [49]. We also fix $B_0 = 0.01$ as described above (results depend weakly on this parameter). We vary the dimensionless parameters $\varepsilon_0, \sigma_0, t_w$ to control the structure of the gel samples and explore their response to applied stress. We control the system size by varying N, keeping all other dimensionless parameters fixed, finding weak finite-size effects.

The same model was compared directly with experiments on colloidal gels [49]. The mean colloid diameter was 460 nm in that study, with a Brownian time of 32 ms. In this case the time scales of order $10^4\tau_B$ considered in this work correspond to a few minutes of experimental time, and a stress $\sigma_0 = 1$ corresponds to approximately 0.04 Pa. Smaller colloids (say 100 nm) would have smaller Brownian times so $10^4\tau_B$ would be a few seconds, and the corresponding stresses would be larger (∼4 Pa).

APPENDIX B: ALGORITHM FOR DETECTION OF STRAND-BREAKING EVENTS

This appendix describes our algorithm for detection of strand-breaking events, including how we avoid false-positive results.

The gel is a complex topological object with load-bearing strands whose thickness and length are highly dependent on interaction strength and preparation history. Upon shear deformation, such a strand experiences force, becomes thin with the formation of the neck, and ultimately breaks. Detection of such events is nontrivial because particles are always moving due to thermal fluctuations, leading to structural relaxation within strands and diffusion of surface particles, as well as strand breaking. For example, thermal fluctuations occasionally lead to particles "desorbing" from the surface of a strand and diffusing through the void spaces.

To specifically detect strand-breaking events and exclude desorption, we rely on a topological measure, which is the chemical distance ℓ_d [23]. To calculate this, we define *bonds* by identifying particles separated by less than the interaction cutoff r_c. A bonded cluster is a set of particles connected by bonds. If two particles i and j are in the same cluster, they must be connected by a path, formed by a set of bonds. Their chemical distance ℓ_d is the number of bonds in the shortest such path. For example, bonded (neighboring) particles have $\ell_d = 1$ and next-nearest neighbors have $\ell_d = 2$, etc.

When a strand breaks, the pair of neighboring particles at the breaking point will have a sudden jump $\Delta\ell_d$ in their chemical distance, from $\ell_d = 1$ to some larger value. We introduce a threshold to detect these events, which is $\Delta\ell_d > 6$ (see, however, below). For simplicity of calculation, we insist that particles that have already participated in breaking events cannot be involved in any later ones.

The threshold for $\Delta\ell_d$ ensures that particle rearrangements within a single strand are not incorrectly identified as strand-breaking events. However, we found that the algorithm described so far leads to some false-positive results for strand breaking. This can happen for desorption events as defined above, in which case the chemical distance after desorption is

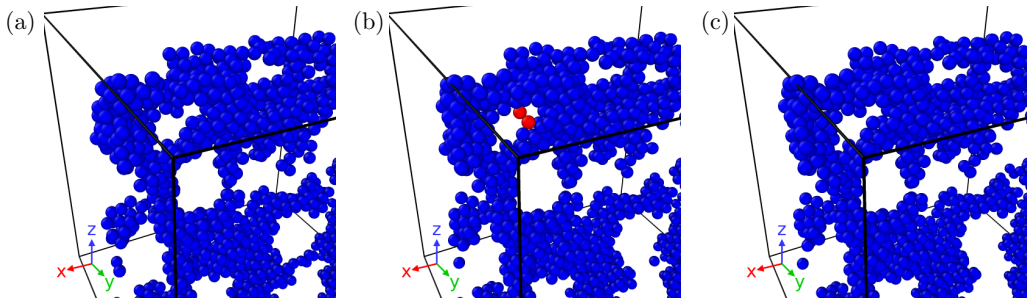

FIG. 12. A part of the system at a different time of simulation showing two arms that are away before [shown in (a)], come closer and particles from each arm (in red) become a neighboring pair [shown in (b)], and a later time when those two particles move apart [shown in (c)]. Even though $\Delta\ell_d > 6$ at the breaking time, our algorithm does not detect this as a breaking event.

infinite. We therefore exclude such events and insist that the chemical distance has a finite jump.

Another type of false-positive event occurs when two strands temporarily approach each other, such that bonds form between their constituent particles, but these bonds are quickly broken. An example is shown in Fig. 12. Similar transient formation of neighboring pairs can also happen due to the diffusion of nearby particles. To avoid this, we modified our criterion to enforce that the relevant particles were neighbors for a sufficiently long time before the event, and remain separate for a sufficiently long time after it. That is, we require that $\Delta\ell_d > 6$ at the breaking time t_b and that the particles have $\ell_d = 1$ for $t_b - \delta t < t < t_b$, and that $\ell_d > 1$ for $t_b < t < t_b + \delta t$, where δt is another threshold parameter. We take $\delta t = 20\tau$; results depend weakly on this parameter. Inspection of the bond-breaking events detected by this method shows that they have the correct topological structure, as seen in Fig. 2.

APPENDIX C: SPATIALLY UNCORRELATED STRAND-BREAKING EVENTS

In the main text, we explained that there is no spatial correlation in the location of the strand-breaking events [Fig. 2(f)]. Figures 13(a)–13(c) show additional snapshots of the location of the breaking events at different times. We see that the points are scattered in space and there is no apparent spatial correlation between them. To quantify the correlation, we compute the radial distribution function of the breaking points after some number of events, n_{events}. In Fig. 13(d) we show the radial distribution of the location of events for different n_{events}. The distribution exhibits ideal gas behavior for the whole range of r, inferring the uncorrelated nature of event location.

APPENDIX D: DEFINITIONS OF STRUCTURAL METRICS

This appendix provides detailed definitions of structural measurements. The formulas are taken from the literature; they are collected here for completeness.

To characterize strand-breaking events we compute twofold bond orientational order parameter q_2 [75], nonaffine displacement D^2_{min} [63], and stress anisotropy J_2 of local stress computed by Irving and Kirkwood's method [29,64,76,77]. We also perform topological cluster classification [61] to extract the structural information. All these quantities are single-particle measurements, as we now explain.

1. Bond orientational order parameter

The bond orientational order parameter q_l is calculated as follows [75]:

$$q_l(i) = \sqrt{\frac{4\pi}{2l+1}\sum_{m=-l}^{l}|q_{lm}(i)|^2}, \tag{D1}$$

$$q_{lm}(i) = \frac{1}{N_b(i)}\sum_{j=1}^{N_b(i)} Y_{lm}(\mathbf{r}_{ij}), \tag{D2}$$

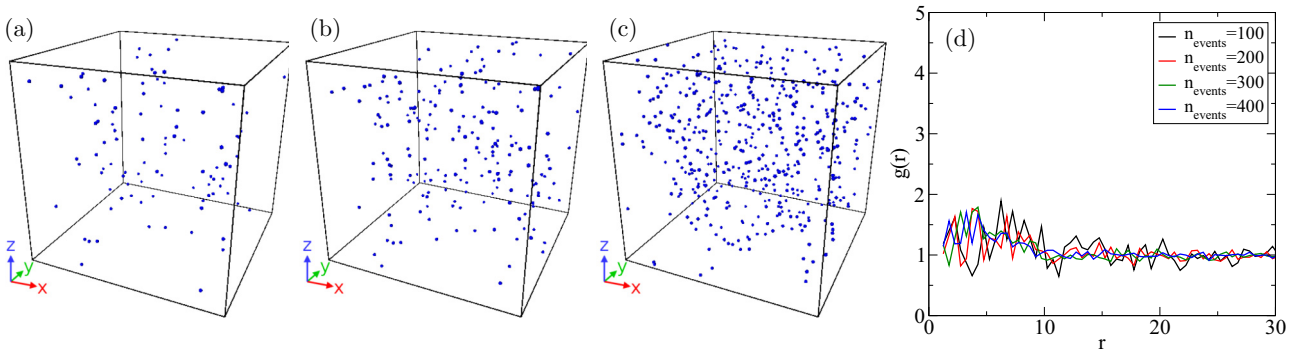

FIG. 13. (a)–(c) Snapshots of locations of the strand-breaking events after $n_{\text{events}} = 100, 200, 400$, respectively. [See also the inset of Fig. 2(f).] (d) Radial distribution function of the location of strand-breaking events after different number of n_{events}.

where Y_{lm} are spherical harmonics and $N_b(i)$ is the number of neighbors of reference particle i. We consider the case $l = 2$ when the quantity q_2 measures the stretching of a bond between two particles. Particles within the interaction range of particle i are defined as its neighbor, and such definition is maintained for all the computations.

2. Nonaffine displacement

We consider nonaffine displacement $D^2_{\rm min}$ per particle to quantify plasticity in the system. The nonaffine displacement of a particle i from time t to $t + \Delta t$ is defined as [63]

$$D^2_{\rm min}(i)(t, \Delta t) = \sum_{j,\alpha} \Big(r^\alpha_j(t) - r^\alpha_i(t) - \sum_\beta (\delta_{\alpha\beta} + \varepsilon_{\alpha\beta}) \times \big[r^\beta_j(t - \Delta t) - r^\beta_i(t - \Delta t)\big]\Big)^2, \quad \text{(D3)}$$

where the indices α and β stand for the spatial coordinates and the index j runs over $N_b(i)$ neighbors of the reference particle i. The local strain $\varepsilon_{\alpha\beta}$, which minimizes $D^2_{\rm min}$, is calculated as

$$X_{\alpha\beta} = \sum_j \big[r^\alpha_j(t) - r^\alpha_i(t)\big]\big[r^\beta_j(t - \Delta t) - r^\beta_i(t - \Delta t)\big],$$
$$Y_{\alpha\beta} = \sum_j \big[r^\alpha_j(t - \Delta t) - r^\alpha_i(t - \Delta t)\big] \times \big[r^\beta_j(t - \Delta t) - r^\beta_i(t - \Delta t)\big],$$
$$\varepsilon_{\alpha\beta} = \sum_\gamma X_{\alpha\gamma} Y^{-1}_{\gamma\beta} - \delta_{\alpha\beta}. \quad \text{(D4)}$$

We choose $\Delta t = 1$.

3. Stress anisotropy

We measure local stress using a volume-averaged representation of the Irving-Kirkwood (IK) stress [29,64,76,77]. Denoting p_i as the momentum of particle i, r_{ij} is the vector connecting particles i and j, and f_{ij} the corresponding interparticle force, for a spatial region with volume $|\Omega|$, the $\mu\nu$ component of the IK stress is defined as

$$\sigma^{\mu\nu}_{|\Omega|} = -\frac{1}{|\Omega|}\left[\sum_{i=1}^{N} \frac{1}{m_i} p^\mu_i p^\nu_i \theta_{i,\Omega} + \frac{1}{2}\sum_i^N \sum_{j\neq i}^N r^\mu_{ij} f^\nu_i \phi_{ij,\Omega}\right], \quad \text{(D5)}$$

where $\theta_{i,\Omega} = 1$ if particle i is in Ω and zero otherwise; similarly, $\phi_{ij,\Omega}$ is the fraction of the straight line connecting particles i, j that lies within Ω. Taking Ω to be the entire simulation box L^3 gives the total stress σ, which can also be computed from the virial. In practice to measure the local stress $\sigma_\Omega(r)$ at point r, we take Ω as a small cube of side $l_{\rm IK}$, centered at r. We choose $l_{\rm IK} = 1.5$. To eliminate the noisy behavior due to thermal fluctuations we average the stress value over a period of 20τ [29] and then do the subsequent measurements.

We consider the second invariant $J_{2,\Omega}$ of the stress tensor to measure the anisotropy of the stress in local volume Ω as

$$J_{2,\Omega} = \tfrac{1}{2}\mathrm{tr}\Big(\big[\sigma_\Omega - \tfrac{1}{3}\mathrm{tr}(\sigma_\Omega)\big]^2\Big). \quad \text{(D6)}$$

Large $J_{2,\Omega}$ means there is more anisotropy in the volume Ω while a value zero means the volume Ω behaves like a simple fluid. We also note that since $J_{2,\Omega}$ is a scalar quantity, it is independent of the orientation of the coordinate system. Particles in the volume Ω are assigned to have $J_{2,\Omega}$ value.

4. Topological cluster classification

To investigate the structural change in the system, we perform topological cluster classification. For each particle i, we compute (a) its number of neighbors N_b; (b) the number of fully bonded tetrahedra in which it participates, $n_{\rm tet}$; and (c) the numbers of trigonal pyramids in which it participates, $n_{\rm tb}$. All the parameters of the TCC are kept the same as [61].

APPENDIX E: DEPENDENCE OF THE GEL ON $\varepsilon_{0,\rm prep}$ AND $t_{\rm w}$

1. Measurement method for strand thickness and pore size

Figure 9 shows how the gel structure depends on $t_{\rm w}$, for different $\varepsilon_{0,\rm prep}$. Following [68], we measure the distribution of pore sizes in the gel and we also adapt their method to measure the distribution of strand thicknesses. For the pore size $D_{\rm pore}$, we take a random point in the gel and we find the largest possible sphere that includes that point, without overlapping with any colloidal particles. If the sphere is larger than $\bar{\ell}$, then we say that the random point lies inside a pore and we identify $D_{\rm pore}$ as the diameter of the sphere. By repeating this process for many random points, we build up the distribution of pore sizes. (Larger pores appear in the distribution with weight proportional to their volume.)

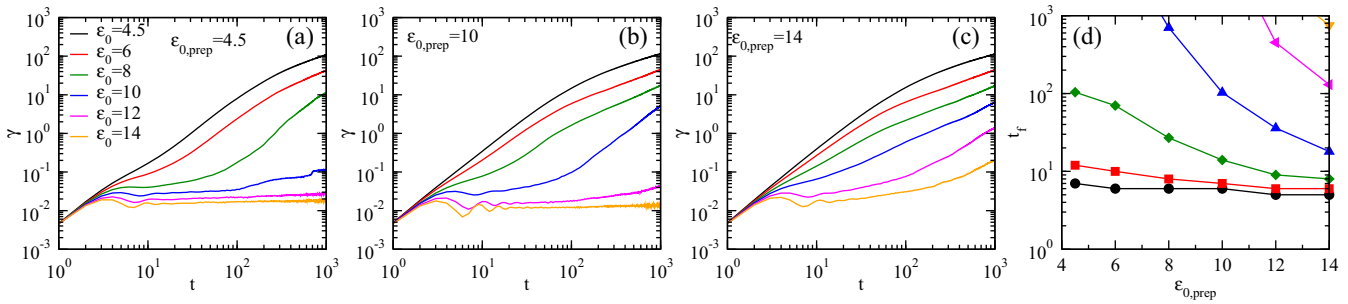

FIG. 14. Strain against time for different ε_0 during shear for a gel prepared with (a) $\varepsilon_{0,\rm prep} = 4.5$, (b) $\varepsilon_{0,\rm prep} = 10$, and (c) $\varepsilon_{0,\rm prep} = 14$. (d) Failure time $t_{\rm f}$ as a function of $\varepsilon_{0,\rm prep}$ for several ε_0. The legend in (a) is common to all panels.

To measure the distribution of strand thickness D_{strand}, we discretize the simulation box into cubic cells of size approximately $\bar{\ell}/2$, and define the "void space" to include all cells whose central point is more than $\bar{\ell}/2$ from the center of any particle. The "colloid space" is the complement of the void space. Then we adapt the pore-size characterization as follows: we choose a random point in the colloid space and find the largest sphere that includes the random point but does not overlap any part of the void space. The diameter of this sphere is the strand thickness D_{strand}.

2. Creeping flow for different $\varepsilon_{0,\text{prep}}$

Recall from Fig. 10(b) that the failure time t_f depends significantly on the preparation protocol of the gel. Figure 14 explores these effects in more detail. Figures 14(a), 14(b), and 14(c) show the strain evolution for three different gels, prepared with different $\varepsilon_{0,\text{prep}}$. To reduce numerical computation, we simulate times $t \leqslant 10^3$ and relax the condition of the definition of failure time by taking t_f as the time to reach $\gamma = 0.1$. In Fig. 14(d) we plot the resulting t_f as a function of ε_0 and $\varepsilon_{0,\text{prep}}$.

[1] E. Zaccarelli, Colloidal gels: Equilibrium and non-equilibrium routes, J. Phys.: Condens. Matter **19**, 323101 (2007).

[2] C. P. Royall, M. A. Faers, S. L. Fussell, and J. E. Hallett, Real space analysis of colloidal gels: Triumphs, challenges and future directions, J. Phys.: Condens. Matter **33**, 453002 (2021).

[3] L. Cipelletti and L. Ramos, Slow dynamics in glassy soft matter, J. Phys.: Condens. Matter **17**, R253 (2005).

[4] W. C. K. Poon, The physics of a model colloid–polymer mixture, J. Phys.: Condens. Matter **14**, R859 (2002).

[5] P. J. Lu, E. Zaccarelli, F. Ciulla, A. B. Schofield, F. Sciortino, and D. A. Weitz, Gelation of particles with short-range attraction, Nature (London) **453**, 499 (2008).

[6] R. Mezzenga, P. Schurtenberger, A. Burbidge, and M. Michel, Understanding foods as soft materials, Nat. Mater. **4**, 729 (2005).

[7] Z. Xiong, X. Yun, L. Qiu, Y. Sun, B. Tang, Z. He, J. Xiao, D. Chung, T. W. Ng, H. Yan, R. Zhang, X. Wang, and D. Li, A dynamic graphene oxide network enables spray printing of colloidal gels for high-performance micro-supercapacitors, Adv. Mater. **31**, 1804434 (2019).

[8] M. Diba, H. Wang, T. E. Kodger, S. Parsa, and S. C. G. Leeuwenburgh, Highly elastic and self-healing composite colloidal gels, Adv. Mater. **29**, 1604672 (2017).

[9] S. Rose, A. Prevoteau, P. Elzière, D. Hourdet, A. Marcellan, and L. Leibler, Nanoparticle solutions as adhesives for gels and biological tissues, Nature (London) **505**, 382 (2014).

[10] D. Bonn, M. M. Denn, L. Berthier, T. Divoux, and S. Manneville, Yield stress materials in soft condensed matter, Rev. Mod. Phys. **89**, 035005 (2017).

[11] T. Divoux *et al.*, Ductile-to-brittle transition and yielding in soft amorphous materials: Perspectives and open questions, Soft Matter **20**, 6868 (2024).

[12] L. Berthier, G. Biroli, M. L. Manning, and F. Zamponi, Yielding and plasticity in amorphous solids, arXiv:2401.09385.

[13] J. O. Cochran, G. L. Callaghan, M. J. G. Caven, and S. M. Fielding, Slow fatigue and highly delayed yielding via shear banding in oscillatory shear, Phys. Rev. Lett. **132**, 168202 (2024).

[14] D. Bonn and M. M. Denn, Yield stress fluids slowly yield to analysis, Science **324**, 1401 (2009).

[15] M. Bouzid, J. Colombo, L. V. Barbosa, and E. Del Gado, Elastically driven intermittent microscopic dynamics in soft solids, Nat. Commun. **8**, 15846 (2017).

[16] S. Aime, L. Ramos, and L. Cipelletti, Microscopic dynamics and failure precursors of a gel under mechanical load, Proc. Natl. Acad. Sci. USA **115**, 3587 (2018).

[17] H. A. Lockwood, M. H. Agar, and S. M. Fielding, Power law creep and delayed failure of gels and fibrous materials under stress, Soft Matter **20**, 2474 (2024).

[18] L. Starrs, W. C. K. Poon, D. J. Hibberd, and M. M. Robins, Collapse of transient gels in colloid-polymer mixtures, J. Phys.: Condens. Matter **14**, 2485 (2002).

[19] P. Bartlett, L. J. Teece, and M. A. Faers, Sudden collapse of a colloidal gel, Phys. Rev. E **85**, 021404 (2012).

[20] Z. Varga, J. L. Hofmann, and J. W. Swan, Modelling a hydrodynamic instability in freely settling colloidal gels, J. Fluid Mech. **856**, 1014 (2018).

[21] A. D. Dinsmore, V. Prasad, I. Y. Wong, and D. A. Weitz, Microscopic structure and elasticity of weakly aggregated colloidal gels, Phys. Rev. Lett. **96**, 185502 (2006).

[22] L. C. Hsiao, R. S. Newman, S. C. Glotzer, and M. J. Solomon, Role of isostaticity and load-bearing microstructure in the elasticity of yielded colloidal gels, Proc. Natl. Acad. Sci. USA **109**, 16029 (2012).

[23] H. Tsurusawa, M. Leocmach, J. Russo, and H. Tanaka, Direct link between mechanical stability in gels and percolation of isostatic particles, Sci. Adv. **5**, eaav6090 (2019).

[24] M. Bantawa, B. Keshavarz, M. Geri, M. Bouzid, T. Divoux, G. H. McKinley, and E. D. Gado, The hidden hierarchical nature of soft particulate gels, Nat. Phys. **19**, 1178 (2023).

[25] M. Nabizadeh, F. Nasirian, X. Li, Y. Saraswat, R. Waheibi, L. C. Hsiao, D. Bi, B. Ravandi, and S. Jamali, Network physics of attractive colloidal gels: Resilience, rigidity, and phase diagram, Proc. Natl. Acad. Sci. USA **121**, e2316394121 (2024).

[26] D. Mangal, M. Nabizadeh, and S. Jamali, Predicting yielding in attractive colloidal gels, Phys. Rev. E **109**, 014602 (2024).

[27] J. M. van Doorn, J. E. Verweij, J. Sprakel, and J. van der Gucht, Strand plasticity governs fatigue in colloidal gels, Phys. Rev. Lett. **120**, 208005 (2018).

[28] J. E. Verweij, F. A. M. Leermakers, J. Sprakel, and J. Van Der Gucht, Plasticity in colloidal gel strands, Soft Matter **15**, 6447 (2019).

[29] K. Thijssen, T. B. Liverpool, C. P. Royall, and R. L. Jack, Necking and failure of a particulate gel strand: Signatures of yielding on different length scales, Soft Matter **19**, 7412 (2023).

[30] J. Sprakel, S. B. Lindström, T. E. Kodger, and D. A. Weitz, Stress enhancement in the delayed yielding of colloidal gels, Phys. Rev. Lett. **106**, 248303 (2011).

[31] S. B. Lindström, T. E. Kodger, J. Sprakel, and D. A. Weitz, Structures, stresses, and fluctuations in the delayed failure of colloidal gels, Soft Matter **8**, 3657 (2012).

[32] J. Colombo and E. Del Gado, Stress localization, stiffening, and yielding in a model colloidal gel, J. Rheol. **58**, 1089 (2014).
[33] B. J. Landrum, W. B. Russel, and R. N. Zia, Delayed yield in colloidal gels: Creep, flow, and re-entrant solid regimes, J. Rheol. **60**, 783 (2016).
[34] B. Saint-Michel, T. Gibaud, and S. Manneville, Predicting and assessing rupture in protein gels under oscillatory shear, Soft Matter **13**, 2643 (2017).
[35] C. P. Royall, S. R. Williams, T. Ohtsuka, and H. Tanaka, Direct observation of a local structural mechanism for dynamic arrest, Nat. Mater. **7**, 556 (2008).
[36] S. Griffiths, F. Turci, and C. P. Royall, Local structure of percolating gels at very low volume fractions, J. Chem. Phys. **146**, 014905 (2017).
[37] F. J. Müller, L. Isa, and J. Vermant, Toughening colloidal gels using rough building blocks, Nat. Commun. **14**, 5309 (2023).
[38] D. Mangal, G. S. Vera, S. Aime, and S. Jamali, Small variations in particle-level interactions lead to large structural heterogeneities in colloidal gels, Soft Matter **20**, 4692 (2024).
[39] P. Coussot, Q. D. Nguyen, H. T. Huynh, and D. Bonn, Avalanche behavior in yield stress fluids, Phys. Rev. Lett. **88**, 175501 (2002).
[40] P. Coussot, Q. D. Nguyen, H. T. Huynh, and D. Bonn, Viscosity bifurcation in thixotropic, yielding fluids, J. Rheol. **46**, 573 (2002).
[41] R. N. Zia, B. J. Landrum, and W. B. Russel, A micro-mechanical study of coarsening and rheology of colloidal gels: Cage building, cage hopping, and smoluchowski's ratchet, J. Rheol. **58**, 1121 (2014).
[42] N. Koumakis, E. Moghimi, R. Besseling, W. C. K. Poon, J. F. Brady, and G. Petekidis, Tuning colloidal gels by shear, Soft Matter **11**, 4640 (2015).
[43] P. J. M. Swinkels, R. Sinaasappel, Z. Gong, S. Sacanna, W. V. Meyer, F. Sciortino, and P. Schall, Networks of limited-valency patchy particles, Phys. Rev. Lett. **132**, 078203 (2024).
[44] K. Ioannidou, M. Kanduč, L. Li, D. Frenkel, J. Dobnikar, and E. Del Gado, The crucial effect of early-stage gelation on the mechanical properties of cement hydrates, Nat. Commun. **7**, 12106 (2016).
[45] S. M. Fenton, P. Padmanabhan, B. K. Ryu, T. T. D. Nguyen, R. N. Zia, and M. E. Helgeson, Minimal conditions for solidification and thermal processing of colloidal gels, Proc. Natl. Acad. Sci. USA **120**, e2215922120 (2023).
[46] L. Cipelletti, S. Manley, R. C. Ball, and D. A. Weitz, Universal aging features in the restructuring of fractal colloidal gels, Phys. Rev. Lett. **84**, 2275 (2000).
[47] R. Rice, R. Roth, and C. P. Royall, Polyhedral colloidal rocks: Low-dimensional networks, Soft Matter **8**, 1163 (2012).
[48] I. Zhang, C. P. Royall, M. A. Faers, and P. Bartlett, Phase separation dynamics in colloid-polymer mixtures: The effect of interaction range, Soft Matter **9**, 2076 (2013).
[49] A. Razali, C. J. Fullerton, F. Turci, J. E. Hallett, R. L. Jack, and C. P. Royall, Effects of vertical confinement on gelation and sedimentation of colloids, Soft Matter **13**, 3230 (2017).
[50] J. Taffs, A. Malins, S. R. Williams, and C. P. Royall, A structural comparison of models of colloid-polymer mixtures, J. Phys.: Condens. Matter **22**, 104119 (2010).
[51] M. Leocmach, C. Perge, T. Divoux, and S. Manneville, Creep and fracture of a protein gel under stress, Phys. Rev. Lett. **113**, 038303 (2014).
[52] S. Asakura and F. Oosawa, On interaction between 2 bodies immersed in a solution of macromolecules, J. Chem. Phys. **22**, 1255 (1954).
[53] C. P. Royall, J. Eggers, A. Furukawa, and H. Tanaka, Probing colloidal gels at multiple length scales: The role of hydrodynamics, Phys. Rev. Lett. **114**, 258302 (2015).
[54] J. de Graaf, W. C. K. Poon, M. J. Haughey, and M. Hermes, Hydrodynamics strongly affect the dynamics of colloidal gelation but not gel structure, Soft Matter **15**, 10 (2019).
[55] M. G. Noro and D. Frenkel, Extended corresponding-states behavior for particles with variable range attractions, J. Chem. Phys. **113**, 2941 (2000).
[56] T. A. Vezirov, S. Gerloff, and S. H. L. Klapp, Manipulating shear-induced non-equilibrium transitions in colloidal films by feedback control, Soft Matter **11**, 406 (2015).
[57] R. Cabriolu, J. Horbach, P. Chaudhuri, and K. Martens, Precursors of fluidisation in the creep response of a soft glass, Soft Matter **15**, 415 (2019).
[58] S. L. Taylor, R. Evans, and C. P. Royall, Temperature as an external field for colloid–polymer mixtures: Quenching by heating and melting by cooling, J. Phys.: Condens. Matter **24**, 464128 (2012).
[59] I. Procaccia, C. Rainone, and M. Singh, Mechanical failure in amorphous solids: Scale-free spinodal criticality, Phys. Rev. E **96**, 032907 (2017).
[60] R. L. Moorcroft and S. M. Fielding, Criteria for shear banding in time-dependent flows of complex fluids, Phys. Rev. Lett. **110**, 086001 (2013).
[61] A. Malins, S. R. Williams, J. Eggers, and C. P. Royall, Identification of structure in condensed matter with the topological cluster classification, J. Chem. Phys. **139**, 234506 (2013).
[62] See Supplemental Material at http://link.aps.org/supplemental/10.1103/PhysRevE.111.055412 for a movie of a gel with $\varepsilon_0 = 10$ showing the strain as a function of time, together with animations of the whole gel, and a slice through it. The shapshots are color-coded according to coordination number N_b, bond-orientation parameter q_2, stress anisotropy J_2, and nonaffine displacement (between time 0 and t). We show times such that $0 \leqslant \gamma \lesssim 0.5$.
[63] M. L. Falk and J. S. Langer, Dynamics of viscoplastic deformation in amorphous solids, Phys. Rev. E **57**, 7192 (1998).
[64] J. H. Irving and J. G. Kirkwood, The statistical mechanical theory of transport processes. IV. the equations of hydrodynamics, J. Chem. Phys. **18**, 817 (1950).
[65] F. Sausset, G. Biroli, and J. Kurchan, Do solids flow? J. Stat. Phys. **140**, 718 (2010).
[66] C. Liu, K. Martens, and J.-L. Barrat, Mean-field scenario for the athermal creep dynamics of yield-stress fluids, Phys. Rev. Lett. **120**, 028004 (2018).
[67] B. P. Bhowmik, H. G. E. Hentschel, and I. Procaccia, Creep failure of amorphous solids under tensile stress, Phys. Rev. E **106**, 034906 (2022).
[68] L. D. Gelb and K. E. Gubbins, Pore size distributions in porous glasses: A computer simulation study, Langmuir **15**, 305 (1999).
[69] S. M. Fielding, Shear banding in soft glassy materials, Rep. Prog. Phys. **77**, 102601 (2014).
[70] A. Nicolas, E. E. Ferrero, K. Martens, and J.-L. Barrat, Deformation and flow of amorphous solids: Insights from elastoplastic models, Rev. Mod. Phys. **90**, 045006 (2018).

[71] C. P. Royall and A. Malins, The role of quench rate in colloidal gels, Faraday Discuss. **158**, 301 (2012).

[72] D. Klotsa and R. L. Jack, Controlling crystal self-assembly using a real-time feedback scheme, J. Chem. Phys. **138**, 094502 (2013).

[73] X. Tang, B. Rupp, Y. Yang, T. D. Edwards, M. A. Grover, and M. A. Bevan, Optimal feedback controlled assembly of perfect crystals, ACS Nano **10**, 6791 (2016).

[74] A. P. Thompson, H. M. Aktulga, R. Berger, D. S. Bolintineanu, W. M. Brown, P. S. Crozier, P. J. in 't Veld, A. Kohlmeyer, S. G. Moore, T. D. Nguyen, R. Shan, M. J. Stevens, J. Tranchida, C. Trott, and S. J. Plimpton, LAMMPS - a flexible simulation tool for particle-based materials modeling at the atomic, meso, and continuum scales, Comput. Phys. Commun. **271**, 108171 (2022).

[75] P. J. Steinhardt, D. R. Nelson, and M. Ronchetti, Bond-orientational order in liquids and glasses, Phys. Rev. B **28**, 784 (1983).

[76] J. Z. Yang, X. Wu, and X. Li, A generalized irving–kirkwood formula for the calculation of stress in molecular dynamics models, J. Chem. Phys. **137**, 134104 (2012).

[77] E. R. Smith, D. M. Heyes, and D. Dini, Towards the irving-kirkwood limit of the mechanical stress tensor, J. Chem. Phys. **146**, 224109 (2017).